

Deep learning and whole-brain networks for biomarker discovery: modeling the dynamics of brain fluctuations in resting-state and cognitive tasks

Facundo Roffet^{1,2}, Gustavo Deco^{3,4}, Claudio Delrieux^{1,2}, and Gustavo Patow^{3,5,*}

¹Department of Electric and Computer Engineering, Universidad Nacional del Sur, Bahía Blanca, Argentina

²Institute of Computer Science and Engineering, National Scientific and Technological Research Council of Argentina (CONICET), Argentina

³Center for Brain and Cognition, Computational Neuroscience Group, Department of Information and Communication Technologies, Universitat Pompeu Fabra, Barcelona, Spain

⁴Institució Catalana de la Recerca i Estudis Avançats (ICREA), Barcelona, Spain

⁵ViRVIG, University of Girona, Girona, Spain

*gustavo.patow@udg.edu

ABSTRACT

Background: Brain network models offer insights into brain dynamics, but the utility of model-derived bifurcation parameters as biomarkers remains underexplored.

Objective: This study evaluates bifurcation parameters from a whole-brain network model as biomarkers for distinguishing brain states associated with resting-state and task-based cognitive conditions.

Methods: Synthetic BOLD signals were generated using a supercritical Hopf brain network model to train deep learning models for bifurcation parameter prediction. Inference was performed on Human Connectome Project data, including both resting-state and task-based conditions. Statistical analyses assessed the separability of brain states based on bifurcation parameter distributions.

Results: Bifurcation parameter distributions differed significantly across task and resting-state conditions ($p < 0.0001$ for all but one comparison). Task-based brain states exhibited higher bifurcation values compared to rest.

Conclusion: Bifurcation parameters effectively differentiate cognitive and resting states, warranting further investigation as biomarkers for brain state characterization and neurological disorder assessment.

1 Introduction

Non-invasive neuroimaging techniques are becoming widespread, providing a rich information source that revolutionized the study of brain dynamics, enabling researchers to correlate brain activity with observable behaviors and cognitive processes among other goals^{1,2}. Functional magnetic resonance imaging (fMRI), in particular, provides detailed high-resolution spatiotemporal data of oxygen consumption, arguably related to regional brain activity. However, interpreting these data remains a major challenge, as the complexity of brain signals often requires advanced computational approaches and an adequate understanding thereof to uncover meaningful patterns or to elucidate among possible interpretations. Deep learning has emerged as a powerful tool for this purpose^{3,4}, offering flexible models that can learn complex structures directly from raw data without extensive handcrafted features—they learn directly from the available training samples. These models excel at extracting intricate patterns across diverse domains and have demonstrated their versatility in a wide range of tasks, including classifying handwritten digits⁵, detecting objects in a scene⁶, segmenting brain tumors⁷, playing board games⁸ and bidirectional mapping of structural and functional brain connectivity⁹.

Biomarkers play a crucial role in advancing 4P medicine (predictive, preventive, personalized, and participatory), enabling, among other things, an early detection of health-compromising conditions (especially those preventable or treatable at an early stage), monitoring disease progression, evaluating the effectiveness of treatments, and tailoring treatments to individual needs. Given that 4P medicine is inherently participative, it necessitates the collection of extensive and diverse data from a broad range of individuals to ensure comprehensive insights and effective implementation of personalized healthcare strategies. For this reason, there is an increasing need in neuroscience for adequate and useful biomarkers¹⁰, defined as measurable biological indicators that provide insights to distinguish normal from pathological processes in the brain, or responses to interventions such as therapies or drugs. For instance, fMRI-based biomarkers can detect functional connectivity abnormalities distinguishing Alzheimer’s disease from mild cognitive impairment and healthy controls¹¹. Similarly, Bruin et al.¹² proposed biomarkers

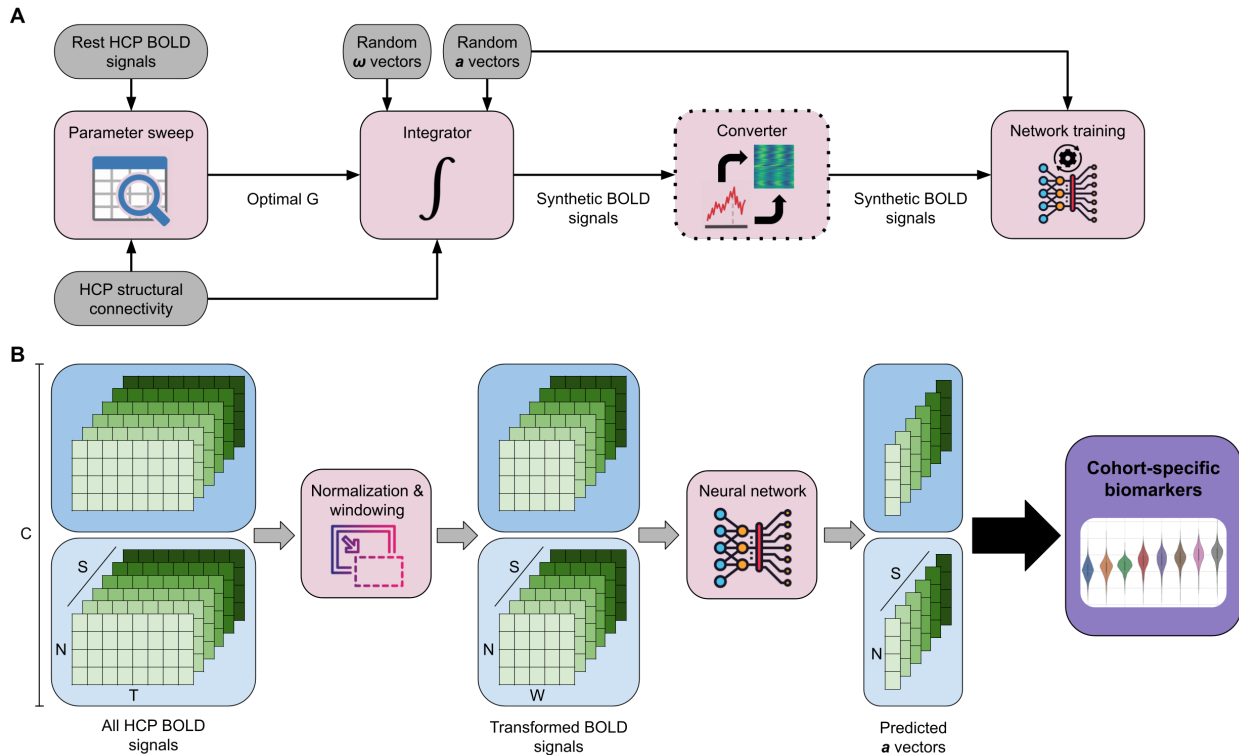


Figure 1. Overview of the training and inference pipelines for predicting bifurcation parameters from BOLD signals.

(A) Synthetic BOLD data is generated using a brain network model based on the supercritical Hopf bifurcation, following a parameter sweep to determine the optimal coupling factor. A deep learning model is trained to predict the bifurcation parameters for each brain node using either a time series or an image-based approach. The converter block, bordered by a dotted line, is used exclusively in the image-based approach. (B) Preprocessed BOLD data from the Human Connectome Project is used to estimate bifurcation parameter values across cohorts. After normalization and windowing, BOLD signals are processed through a trained deep learning model to generate predictions. These predicted values provide insights into the underlying brain states across different tasks and resting conditions. The data dimensionality includes $C = 8$ cohorts, $S = 1,003$ subjects, T scan time steps, and $W = 50$ window time steps. The value of T varies within each scan.

to predict outcomes of electroconvulsive therapy, enabling more precise interventions for patients with treatment-resistant depression.

In this context, whole-brain computational models represent a promising approach to understanding the dynamic processes of the brain. These models simulate large-scale brain networks, capturing complex neural interactions throughout the brain. Whole-brain models have been valuable in various applications, including understanding network-level disruptions in neurological disorders¹³, guiding potential therapeutic interventions¹⁴, and optimizing simulations to achieve high fidelity with limited computational resources¹⁵. An important example is the study by Deco et al.¹⁶ where the parameters of a simple brain network model were optimized, identifying a *dynamical cortical core* responsible for driving activity across the brain. Although this approach provided valuable insights, the model parameters were not considered as biomarkers for specific brain states or cognitive functions, thereby limiting their generalizability and broader applicability.

To this avail, the present study aims to bridge this gap using a whole-brain computational model to explore whether constructive parameters can be biomarkers for different task-based brain states. In particular, we focus on a *neural mass model*, a mathematical framework that simulates the activity of large groups of neurons, which is capable of capturing the fluctuations in brain activity and transitions between brain states^{17,18}. This model enables to characterize the brain's dynamical system through bifurcation parameters, which describe the shifts in the brain's stability and oscillatory patterns. Our claim is that these bifurcation parameters may be sufficient to characterize distinct task-based brain states associated with various cognitive tasks. We trained deep learning models to predict bifurcation parameters using synthetic BOLD signals generated with Hopf's brain network model (see Fig. 1). By leveraging synthetic data, we overcome the limitations of scarce labeled datasets and ensure that our models are trained on a standardized, well-controlled set of inputs. We then applied the trained models to the Human

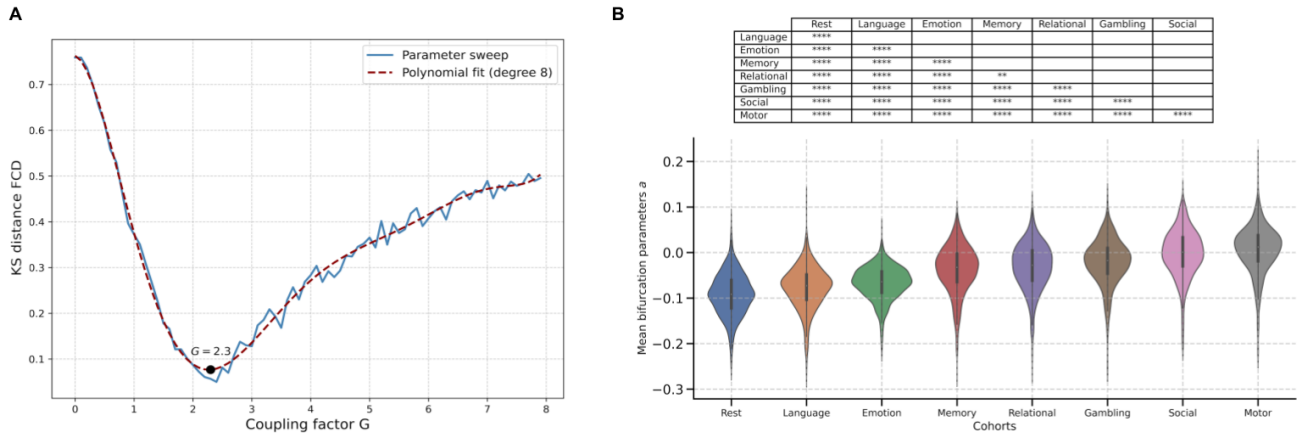


Figure 2. Determination of optimal coupling factor G and statistical comparison of bifurcation parameters across cohorts. (A) The optimal global coupling factor G was estimated through a parameter sweep, minimizing the Kolmogorov-Smirnov distance between the FCD of empirical and simulated BOLD data. The polynomial fit identifies the G value that best aligns the simulated data with the observed resting-state FCD patterns. (B) Distribution of mean bifurcation parameter values across different cognitive task and resting-state cohorts. Statistical significance between cohorts is assessed using the Mann-Whitney-Wilcoxon test, with Benjamini-Hochberg correction applied to control for multiple comparisons. Statistical significance is indicated by **** for $p \leq 0.0001$, *** for $0.0001 < p \leq 0.001$, ** for $0.001 < p \leq 0.01$, * for $0.01 < p \leq 0.05$ and "ns" for $0.05 < p \leq 1$. These results reveal distinguishable brain state characteristics associated with each cognitive task.

Connectome Project (HCP) dataset to estimate bifurcation parameter distributions across cohorts performing different cognitive tasks. By comparing these distributions, we investigate whether bifurcation parameters can serve as meaningful brain state indicators, potentially offering a novel approach to mapping cognitive functions through model-driven biomarkers.

2 Results

This study examined brain dynamics across multiple cognitive tasks using data from the HCP, covering seven task-based conditions and resting-state data. Brain imaging data were processed using standard pipelines and segmented into 80 regions of interest (ROIs) with cortical and subcortical coverage using the DBS80 parcellation. We used a brain network model based on the supercritical Hopf bifurcation to model neural activity, simulating interactions among these brain regions. Model parameters, such as global coupling factor (G) and intrinsic oscillation frequencies (ω_j), were calibrated to match the phase functional connectivity dynamics (FCD) observed in the HCP resting-state data. Given the limited sample size for training a deep learning model, synthetic BOLD signals were generated to create a voluminous dataset, allowing these models to be effectively trained. Thus, deep learning models were trained on synthetic data to predict the model bifurcation parameters a_j for each brain region j from BOLD signals. These values serve as a proxy for brain state characteristics, capturing task-related variations in neural activity across brain regions. The trained models were then applied to empirical HCP data, allowing statistical analysis to identify significant differences across tasks and brain networks, thus providing insights into the underlying brain states associated with each cognitive task.

2.1 Developing of the deep learning models

2.1.1 Optimal coupling factor G

The optimal fit for the HCP dataset is achieved with an intermediate value of the global coupling factor G . Specifically, the Kolmogorov-Smirnov (KS) distance between the empirical and simulated FCD is minimized at $G = 2.3$ (Fig. 2A). Since G scales the elements of the structural connectivity matrix C_{ij} , normalized to a maximum value of 0.2, this implies that the strongest allowed connection between brain nodes is 0.46.

2.1.2 Samples are more important than time steps

We conducted a comprehensive hyperparameter exploration to understand how the dimensions of the synthetic BOLD signals impact the predictive performance of our deep learning models. In this exploration, the number of samples (S), nodes (N), and time steps (W) were jointly adjusted, while ensuring the total size of the dataset did not exceed 160 million values ($S \times N \times W$)

		Samples (S)					
		2,500	5,000	10,000	20,000	40,000	80,000
Time steps (W)	25	14.68	13.11	12.06	11.22	10.68	10.12
	50	13.79	12.47	11.63	10.83	9.82	
	100	13.64	12.50	11.47	11.37		
	200	13.39	12.47	12.00			
	400	13.65	12.47				
	800	13.84					

Table 1. Model performance metrics for different configurations of samples (S) and time steps (W) in the training dataset. Each model was trained using a unique combination of S and W values, with the total dataset size capped at 160 million values ($S \times N \times W$, with $N = 80$ nodes) to ensure computational feasibility. Model performance is evaluated using a normalized version of the root mean squared error (RMSE), with lower values indicating better predictive accuracy. Results indicate that increasing the number of samples leads to more accurate models while increasing time steps has a smaller and inconsistent effect on performance. All models reported in this table were trained using the time series approach.

to maintain a limited computational budget. Since the selected parcellation fixes the number of nodes at $N = 80$, we focused on just varying the values of S and W . For each viable combination of these parameters (i.e., those that remained within the imposed threshold), a separate model was trained using the time series approach. The performance metrics of these models are reported in Table 1.

Our findings confirm that increasing the number of samples consistently improves model performance across all tested configurations. This was expected, as more samples generally provide better results when training deep learning models¹⁹. However, increasing the number of time steps shows inconsistent improvements. Although in some cases a slight boost in performance is noticeable with higher W values, the effect plateaus quickly, and further W increments indeed diminish the performance. These results suggest that the most computationally efficient strategy maximizes the number of samples while keeping the time steps relatively low. Importantly, we observed a performance degradation when the time step count dropped to $W = 25$, indicating that reducing W to this point negatively affects the model’s accuracy. Based on these insights, we selected $W = 50$ and $S = 40,000$ as the optimal working point for all subsequent analyses, balancing performance and computational efficiency.

2.1.3 The image approach yields better results

At the optimal working point ($W = 50$ and $S = 40,000$), we trained an additional model using the image-based approach to predict the bifurcation parameters. This approach resulted in a metric value of 6.93, representing a substantial improvement over the 9.82 achieved by the time series approach (see Table 1 for reference). Therefore, this model was selected for conducting subsequent analyses.

2.2 Analysis of predicted bifurcation parameters from the HCP dataset

2.2.1 Cohort separability

Inference on the HCP dataset reveals distinct patterns in the distribution of mean bifurcation parameters across cohorts, supporting their separability based on brain state characteristics. As detailed in the Methods section, we conducted pairwise comparisons of these distributions, with the results presented in Fig. 2B as violin plots with corresponding Mann-Whitney-Wilcoxon test statistics. *Every* cohort comparison yielded statistically significant distribution differences. Remarkably, all pairwise comparisons except one (memory vs. relational) showed a p-value below 0.0001. The plot further illustrates that most bifurcation parameter values are small negative numbers between -0.1 and 0, indicating a system preference for values in the non-oscillatory behavior of the supercritical Hopf bifurcation¹⁶. The resting-state cohort exhibits noticeably lower bifurcation parameter values overall, supporting the hypothesis that these parameters correlate with brain activity. This suggests that greater oscillatory dynamics are required to couple nodes and enhance inter-regional brain communication as the cognitive demands of a task increase.

2.2.2 Brain network activations vary across tasks

To explore how different brain networks are engaged across functions, we grouped cortical nodes according to their respective brain networks, as defined by the Yeo atlas, and averaged bifurcation parameter values within each cohort. After subtracting the resting-state values from each task, we obtained the difference of mean bifurcation parameters shown in Fig. 3. Overall, most

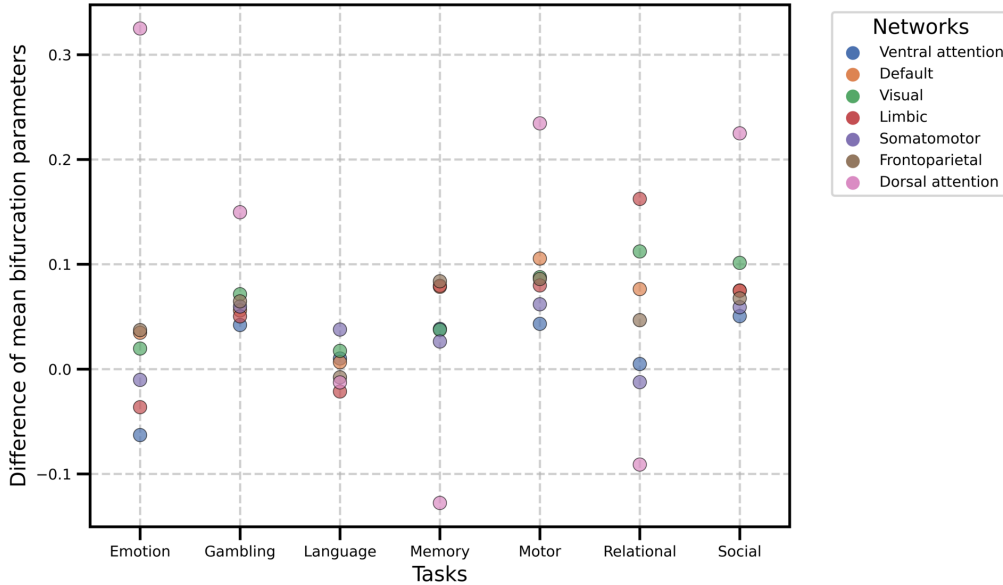


Figure 3. Task-based differences in mean bifurcation parameters across brain networks. The mean bifurcation parameter values were calculated across cortical nodes grouped by brain network using the Yeo atlas for each task. These values were then normalized by subtracting the corresponding mean bifurcation parameter for the resting-state cohort. Each point represents the average difference per network, with colors indicating specific brain networks.

bifurcation parameter values are positive, confirming that these parameters are generally higher during task engagement than at rest, and indicating a system preference for the oscillatory behavior during tasks. Also, this again supports the hypothesis that bifurcation values correlate with brain activity levels.

Interestingly, the dorsal attention network exhibits a highly variable pattern, showing the highest bifurcation values in four tasks but the lowest in two others. This variability could stem from the fact that few nodes are associated with this network, making it difficult to draw robust conclusions without further data. Excluding dorsal attention, the visual network shows the highest bifurcation values overall, ranking in the top four activations for six out of seven tasks and the top two for four tasks. This result is expected, as visual stimuli were integral to most task designs in the experiments²⁰. Similarly, the default network ranks within the top four activations in all but one task, indicating its consistent engagement across different cognitive demands. In contrast, the ventral attention network shows the lowest activity, ranking last in four tasks.

When analyzing individual tasks, we found that emotion and language tasks show near-zero differences from resting-state bifurcation values, suggesting that these tasks may not be particularly demanding regarding brain activation. In contrast, the gambling, motor, and social tasks exhibit consistently positive bifurcation values across networks, suggesting higher engagement. Additionally, the relational task shows substantial variability in bifurcation values across networks, indicating diverse activation patterns.

3 Discussion

We developed a novel deep-learning-based pipeline that addresses the inverse problem for an ordinary differential equation system, specifically tailored to model BOLD signals. This approach allows us to infer key dynamical parameters of a computational brain network model with remarkable efficiency and precision, relying solely on synthetic data for model training. Our results show that this model-driven inference pipeline can distinguish between different cognitive and resting states in empirical data, providing insights into the underlying brain states and supporting the use of bifurcation parameters as potential biomarkers for neural activity patterns. This capability opens a promising landscape for decoding complex task-related brain states and advancing our understanding of the human neurocognition in a computationally efficient and scalable manner.

Our study addresses a significant challenge in neuroscience: large volumes of training data are typically required for deep learning models to generalize effectively²¹. By generating synthetic BOLD signals derived from a simple whole-brain computational model, we circumvented the limitations associated with scarce or heterogeneous neuroimaging data, offering a controlled, high-volume dataset for training. This approach leverages synthetic data to capture essential aspects of BOLD

dynamics without reliance on extensive empirical datasets, thereby avoiding potential biases from real-world data collection conditions. This methodology strengthens the potential of our model to generalize across datasets, highlighting synthetic data as a viable solution in neuroimaging applications where data scarcity often hinders model development.

Previous work in computational brain network modeling has largely focused on examining the dynamics of the human brain in resting states^{22–25}. In a foundational study, Deco et al.¹⁶ demonstrated that the brain operates at maximum metastability during rest, characterized by continual transitions between functional network states. This metastable behavior is thought to enable optimal integration and segregation of information across regions, facilitating flexible cognitive processing. Building on this foundation, our work extends the application of the computational brain network model to task-related brain states, revealing that constructive parameters of the Hopf model –particularly the bifurcation parameters– can serve as biomarkers to differentiate distinct mental states induced by various cognitive tasks. Fig. 2B illustrates the increasing demand for inter-regional coordination and dynamic coupling as tasks deviate from the resting-state condition, accentuating the brain’s adaptive responses to varying levels of complexity. Additionally, the bifurcation parameters we obtained are predominantly small and negative, supporting the authors’ claim that the brain operates near the edge of bifurcation during rest.

To the best of our knowledge, this study is among the earliest to adopt an image-based approach for processing BOLD time series using deep learning. To date, only Kancharala et al. has employed a similar strategy, using Gramian Angular Fields and Markov Transition Fields to encode BOLD signals into image representations²⁶. That work achieved an 18% improvement in classification accuracy when distinguishing brain states induced by viewing images from standard computer vision datasets, compared to conventional time-series-based approaches. Analogously, we observed nearly a 3% decrease in normalized RMSE for bifurcation parameter prediction when using image-based transformations rather than raw time series, underscoring the advantage of this approach. By transforming temporal dynamics into spatial representations, image-based methods allow models to leverage powerful computer vision architectures adept at extracting intricate spatial features to capture complex temporal patterns across brain regions. Image-based time series methodologies in neuroimaging could pave the way for more robust and accurate tools in functional brain mapping and cognitive state classification.

When analyzing the network-specific task activations shown in Fig. 3, our approach successfully links task-based activation patterns to brain networks commonly associated with these functions, aligning with previous findings in the literature²⁷:

- The default mode network is most active during introspective tasks or passive thought²⁸. Since humans almost always subconsciously process the world around them, it is considered one of the most constantly active main brain networks. Consistently, we observed this network as the second most active across tasks, underscoring its ubiquitous role in internal cognitive processing.
- The frontoparietal network (also named central executive network) enables complex problem-solving by integrating inputs from other networks for high-level cognitive functions, such as flexibility, working memory, and inhibition²⁹. Our results showed that this network showed maximum activation during the memory task among all networks.
- The ventral attention network facilitates attention shifts and responsiveness to new stimuli³⁰. Since participants were focused on specific tasks, this network displayed lower activation levels, reflecting its limited role in maintaining attention.
- The visual network controls sight and pattern recognition. As all tasks involve some form of visual processing, this network consistently displayed high bifurcation parameter values across tasks, reflecting its sustained engagement.
- The somatomotor network manages sensory input and converts it to electrical signals that travel throughout the brain to initiate physical responses³¹. While this network was mostly active during the motor task, its relative activation seems low compared to other networks.
- The limbic network regulates essential functions such as emotional response, behavior, memory, and learning³². Although our methodology captures its expected activity during the memory-related task, it failed to capture a correlation with the emotion task.

However, there are some limitations to our approach. One significant constraint is that the separation achieved between tasks is only valid for group-level analysis. This means that, while we can differentiate between tasks on an aggregate level, it is not feasible to classify new BOLD signals by task type solely based on their bifurcation parameters. As shown in Fig. 2B, bifurcation parameter values do not exhibit sufficient task-specific differentiation to enable robust individual-level classification. The model’s optimization likely emphasizes average task-related patterns rather than individual variability within tasks, which could limit its precision in reconstructing individualized BOLD signals. It is also worth noting that the computational brain network model we used is a mesoscopic, phenomenological model. This model directly simulates measured BOLD dynamics rather than neural activity, meaning that regional coupling is applied at the level of hemodynamic signals rather than neural interactions. Focusing directly on BOLD signals, our model avoids the need for neural signal convolution with a hemodynamic response function, simplifying computations and facilitating direct comparisons with fMRI data.

The approach developed in this study opens promising venues for the study of bifurcation parameters as biomarkers, with potential applications in assessing brain development, neurodegeneration, and treatment efficacy. By establishing their discriminative power, this framework aspires to contribute to the diagnosis and monitoring of neurological conditions. For

instance, since changes in network stability and connectivity are hallmarks of conditions such as Alzheimer’s and Parkinson’s disease^{33,34}, bifurcation parameters might be used to identify early-stage disruptions in brain dynamics that signal the onset or progression of these diseases. Future research will focus on individual-level classifications and clinical translation, particularly for monitoring recovery stages in stroke patients.

4 Methods

4.1 Participants and tasks

This study utilized a sample of 1,003 participants in the March 2017 public release of the Human Connectome Project (HCP). Seven distinct cognitive tasks were examined: working memory, motor, gambling, language, social, emotional, and relational –each designed to engage specific brain regions involved in cognitive and emotional processes. Detailed task descriptions can be found in Barch et al.²⁰

4.2 Image acquisition

All participants were scanned using a Siemens 3-T Connectome-Skyra scanner. The scanning protocol was divided into two sessions: the first focused on working memory, gambling, and motor tasks, while the second included language, social cognition, relational processing, and emotion processing tasks. In addition to these task-based scans, each participant completed a resting-state scan, during which they viewed a bright cross projected on a dark background for around 15 minutes. Comprehensive information about the subjects, scanning protocols, and data preprocessing for both task-based and resting-state sessions is available on the HCP website (<http://www.humanconnectome.org/>).

4.3 Parcellation

Neuroimaging data preprocessing was performed using a widely adopted atlas, supplemented with subcortical regions to enhance anatomical coverage. For a coarser parcellation, the Mindboggle-modified Desikan–Killiany atlas³⁵ was employed. This parcellation segmented the cortex into 62 regions, with 31 regions per hemisphere. Additionally, 18 subcortical regions (nine per hemisphere) were included: hippocampus, amygdala, subthalamic nucleus, globus pallidus internal segment, globus pallidus external segment, putamen, caudate, nucleus accumbens, and thalamus. The final parcellation, known as DBS80, comprised 80 regions and was aligned with the HCP CIFTI *gray ordinates* standard space to ensure precise regional mapping.

4.4 BOLD time series extraction

A detailed description of the preprocessing steps applied to the HCP resting-state and task-based datasets is available on the HCP GitHub repository (<https://github.com/Washington-University/HCPpipelines>). In brief, the HCP preprocessing pipeline was used for resting-state and task-based scans, employing standardized tools such as the FMRIB Software Library, FreeSurfer, and Connectome Workbench^{36,37}. The preprocessing steps included: correction for head motion and spatial distortions, intensity normalization, bias field removal, registration to the T1-weighted structural image, and transformation into a 2 mm Montreal Neurological Institute space. For the resting-state data, the FIX artifact removal procedure was applied. Head motion-related noise was regressed, and structured artifacts were removed using independent component analysis (ICA) denoising and the FIX method. The processed time series for all gray coordinates were projected into the HCP CIFTI *gray ordinates* standard space. These files, accessible via surface-based CIFTI formats, were generated for task-based and resting-state conditions. To extract the average time series for each brain region defined by the DBS80 parcellation, a custom Matlab script was used. This script utilized the `ft_read_cifti` function from the Fieldtrip toolbox³⁸. Additionally, the preprocessing pipeline applied a second-order Butterworth filter with a frequency range of 0.008–0.08 Hz to smooth the BOLD signal for both task-based and resting-state datasets.

4.5 Brain network model

The brain network model is composed of 80 interconnected brain regions (nodes), identified through a parcellation, as described previously. The global dynamics of this network emerge from the interactions among local node dynamics, which are coupled according to an empirically derived anatomical structural connectivity matrix C_{ij} . This matrix, extracted through DTI-based tractography, quantifies the fiber density between cortical regions i and j , scaled to a maximum value of 0.2.

The local dynamics of each node are governed by the normal form of a supercritical Hopf bifurcation, a model capable of capturing the transition from random, asynchronous behavior to sustained oscillatory activity. In Cartesian coordinates, the dynamics of a given node j are described by the following set of equations:

$$\frac{dx_j}{dt} = [a_j - x_j^2 - y_j^2] x_j - \omega_j y_j + G \sum_i C_{ij} (x_i - x_j) \beta \eta_j(t), \quad (1)$$

$$\frac{dy_j}{dt} = [a_j - x_j^2 - y_j^2] y_j + \omega_j x_j + G \sum_i C_{ij} (y_i - y_j) \beta \eta_j(t). \quad (2)$$

Here, $\eta_i(t)$ represents additive Gaussian noise with a standard deviation $\beta = 0.02$. All synaptic connections in the network are scaled uniformly by a global coupling factor G .

This normal form has a supercritical bifurcation at $a_j = 0$, marking a shift in the system's behavior. Specifically, for $a_j < 0$, the local dynamics exhibit a stable fixed point at $x_j = 0$ and $y_j = 0$, which, due to additive noise, corresponds to a low-activity asynchronous state. Conversely, for $a_j > 0$, the dynamics reach a stable limit cycle oscillation with frequency $f = \omega_j/2\pi$. Thus, the bifurcation parameter a_j serves as a control parameter that defines the activity state of each node. By adjusting these parameters, the model can simulate distinct task-related brain states associated with specific cognitive tasks. The BOLD signal of each brain region j is then represented by the variable x_j , which provides a measurable proxy for neural activity.

The coupling between nodes follows a common difference scheme, which approximates the linear part of a general coupling function. This model assumes the weakly coupled oscillator regime, where individual oscillators maintain their intrinsic periodic behavior despite interactions. If the linear coupling component vanishes, higher-order nonlinear terms would need to be included, although such cases fall outside the scope of this study.

4.6 Functional connectivity matrices

Functional connectivity (FC) quantifies the statistical relationship between brain regions. Static FC is computed as the Pearson correlation between the BOLD signals of each pair of brain regions across the entire recording session. This process produces an $N \times N$ matrix, where N is the number of nodes, capturing the average spatial organization of brain activity.

Phase functional connectivity dynamics (FCD), on the other hand, assesses how these spatial correlations evolve. The procedure to compute FCD is briefly as follows. First, the BOLD signal of each node is transformed using the Hilbert transform to extract its phase. Then, the cosine of the phase difference between every pair of nodes is used to generate a series of $N \times N$ phase coherence matrices, one for each of the T time points. The similarity between these phase coherence matrices is evaluated by calculating the cosine similarity between their upper triangular elements, resulting in a final $T \times T$ matrix that describes the temporal evolution of the FC patterns. For further details, readers are encouraged to consult the work of Cabral et al.³⁹. When comparing empirical and simulated FCD statistics, the Kolmogorov-Smirnov (KS) distance is used to quantify the largest difference between the cumulative distribution functions of the two samples.

4.7 Estimation of global coupling factor G and frequencies ω

Intrinsic frequencies ω_j were estimated for each brain region from the empirical data by calculating the average peak frequency of the narrowband-filtered BOLD signals for each brain region (see Subsection 4.4). The global coupling factor G was determined through an optimization procedure using a parameter sweep, see Fig. 2A. This optimization aimed to minimize the KS distance between the FCDs of the empirical resting-state BOLD signals and those generated by the simulated brain network model. Simulations were performed for 20 resting-state subjects, with G values ranging from 0 to 8 in steps of 0.1. All other model parameters, including the average resting-state structural connectivity matrix C_{ij} and the intrinsic frequency vector ω mentioned above, were kept constant. The vector \mathbf{a} , controlling local dynamics, was fixed at -0.02 for all nodes, i.e., $a_j = -0.02$, ensuring the system operated near the Hopf bifurcation, a critical point where oscillations emerge. The resulting curve was smoothed using an eighth-degree polynomial fit after obtaining the KS distance for each G value. This polynomial fit allowed for more precise identification of the optimal G value by locating the minimum KS distance.

4.8 Synthetic data generation

Data scarcity poses a particular challenge in neuroscience, as neuroimaging studies are expensive, time-consuming, and often subject to stringent ethical or legal constraints^{40,41}. Apart from this limitation, there are also requirements to control and assess acquisition-related biases, which can vary significantly between scanners, laboratories, and protocols⁴²⁻⁴⁴. While the HCP dataset is considered large in neuroscience (1003 scans), it falls short in a deep learning context by at least an order of magnitude. Synthetic BOLD signals –closely matching the empirical ones– were generated to address this issue and properly train a model.

The stochastic Euler-Maruyama method (with $\sigma = 0.01$) was used to integrate the system of ordinary differential equations associated with the brain network model, producing S new samples, each consisting of W time steps. For each sample, the bifurcation parameter a_j values were randomly drawn from a uniform distribution between -1 and 1 , and between 0.05 and 0.25 for the intrinsic frequencies ω_j . The structural connectivity matrix C_{ij} and the global coupling factor G were constant throughout all simulations. The initial values of the model variables x_j and y_j were randomly selected from the range $[-1, 1]$. To ensure that only stable, meaningful dynamics were analyzed, each simulated sample's first 100 time points were discarded to

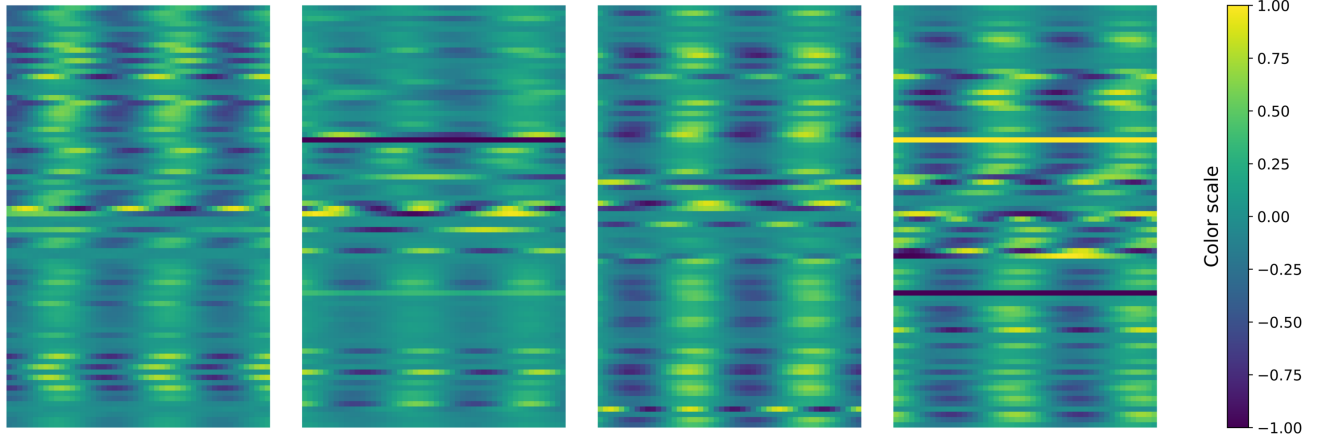


Figure 4. Examples of BOLD time series converted to images for model input in the image-based approach. Each image represents a single window, with height equal to N (the number of nodes) and width equal to W (the number of time steps chosen). The color scale on the right indicates signal values.

eliminate transient effects. Thus, if the desired final sample length is $W = 50$, the simulation must run for 150 time steps. To optimize computational resources during deep learning training, values of S and W were tested, thus determining the most effective configuration (see Table 1).

4.9 Deep learning models for predicting bifurcation parameters

Two regression deep learning models were trained exclusively on synthetic data to predict the bifurcation parameters a_j for each node j from a given BOLD signal, as shown in Fig. 1A. The first model follows a standard time-series approach, treating the BOLD signals as sequential data. The Temporal Convolutional Network (TCN) architecture⁴⁵ was used, with the implementation from the `tsai` Python library (<https://github.com/timeseriesAI/tsai>). In contrast, the second model adopts a more experimental approach by converting each sample into an image before processing. This conversion involves mapping the BOLD values to pixels using a convenient color palette, resulting in a picture with a height of N (the number of nodes) and a width of W (the number of time steps). Randomly selected samples are displayed in Fig.4. This strategy allows to take advantage of current powerful computer vision models, a practice inspired by other deep learning research. Time-series-to-image conversion has previously been applied in various fields, such as audio pattern recognition⁴⁶, algorithmic financial trading⁴⁷, chaotic system classification⁴⁸, and neuronal activity understanding²⁶. In this work, the tiny version of the ConvNeXt architecture⁴⁹ was used, with the implementation provided by the PyTorch Image Models (`timm`) library (<https://github.com/huggingface/pytorch-image-models>).

Both neural networks were trained using an 80/20 split for training and validation data, a batch size of 16, and a learning rate of 0.0003. The mean squared error (MSE) loss function was employed with the Adam optimizer over 30 epochs. The training process utilized the `fit_one_cycle` method from the `FastAI` Python library⁵⁰. The performance of the models was evaluated using a normalized root mean squared error (RMSE) metric, defined as:

$$RMSE_a(\hat{y}, y) = \frac{RMSE(\hat{y}, y) \cdot 100}{a_{max} - a_{min}}, \quad (3)$$

where $a_{max} = 1$ and $a_{min} = -1$, as defined in Subsection 4.8.

4.10 Model inference on the HCP dataset

The HCP BOLD time series were preprocessed before using the trained deep learning models to predict the \mathbf{a} vectors. First, the signals were normalized to a maximum amplitude of 1. Next, the time series from the C cohorts and S subjects were divided into non-overlapping windows of W time steps. For each cohort, the windows belonging to the same subjects were averaged, resulting in a data dimensionality equal to $C \times S \times W \times N$. In the HCP dataset, $S = 1003$ and $C = 8$ (seven tasks plus rest). Since individual scans have varying temporal lengths T , this windowing step ensures that each input conforms to the required size of $N \times W$, where N is the number of nodes, and W is the number of time steps used for model training. The preprocessed BOLD signals are then fed into the neural network, producing predictions for the bifurcation vector \mathbf{a} . The inference pipeline can be visualized in Fig. 1B. For the image-based model, the time-series-to-image conversion step, described earlier, is also applied before feeding the data into the network.

4.11 Comparison across cohorts

The mean a_j values across nodes were calculated to assess differences in bifurcation parameters across cohorts. This operation reduced the data dimensionality from $C \times S \times N$ after inference to $C \times S$. Statistical differences between distributions were evaluated using the Mann-Whitney-Wilcoxon test, with Benjamini-Hochberg correction applied to control the false discovery rate.

4.12 Brain network activations

By interpreting the bifurcation parameters as a proxy for node activation intensity and grouping nodes into brain networks, it is possible to identify which brain regions are generally more active while subjects engage in different tasks. In particular, the Yeo atlas⁵¹ divides the cortical surface into seven networks: default, visual, limbic, somatomotor, frontoparietal, ventral attention, and dorsal attention. First, the mean a -values across subjects were computed, and subcortical nodes were excluded, reducing the data dimensionality from $C \times S \times N$ (cohorts \times subjects \times nodes) to $C \times N'$. In the case of the DBS80 parcellation, $N = 80$ and $N' = 62$. To account for baseline activity, the resting-state cohort was treated as a reference, and its values were subtracted from the corresponding values of each task, resulting in a matrix of size $(C - 1) \times N'$. Finally, the nodes were grouped into the $B = 7$ Yeo brain networks, and the values were averaged within each network, yielding a matrix of size $(C - 1) \times B$.

References

1. Fincham, J. M., Lee, H. S. & Anderson, J. R. Spatiotemporal analysis of event-related fMRI to reveal cognitive states. *Hum. Brain Mapp.* **41**, 666–683, DOI: [10.1002/hbm.24831](https://doi.org/10.1002/hbm.24831) (2020).
2. Yang, Z. & Lewis, L. D. Imaging the temporal dynamics of brain states with highly sampled fMRI. *Curr. Opin. Behav. Sci.* **40**, 87–95, DOI: [10.1016/j.cobeha.2021.02.005](https://doi.org/10.1016/j.cobeha.2021.02.005) (2021).
3. Zhao, Y. *et al.* Automatic Recognition of fMRI-Derived Functional Networks Using 3-D Convolutional Neural Networks. *IEEE Transactions on Biomed. Eng.* **65**, 1975–1984, DOI: [10.1109/TBME.2017.2715281](https://doi.org/10.1109/TBME.2017.2715281) (2018).
4. Thomas, A. W., Lindenberger, U., Samek, W. & Müller, K.-R. Evaluating deep transfer learning for whole-brain cognitive decoding. *J. Frankl. Inst.* **360**, 9754–9787, DOI: [10.1016/j.jfranklin.2023.07.015](https://doi.org/10.1016/j.jfranklin.2023.07.015) (2023).
5. Lecun, Y., Bottou, L., Bengio, Y. & Haffner, P. Gradient-based learning applied to document recognition. *Proc. IEEE* **86**, 2278–2324, DOI: [10.1109/5.726791](https://doi.org/10.1109/5.726791) (1998).
6. Girshick, R. Fast R-CNN (2015). [1504.08083](https://arxiv.org/abs/1504.08083).
7. Havaei, M. *et al.* Brain Tumor Segmentation with Deep Neural Networks (2016). [1505.03540](https://arxiv.org/abs/1505.03540).
8. Silver, D. *et al.* Mastering the game of Go with deep neural networks and tree search. *Nature* **529**, 484–489, DOI: [10.1038/nature16961](https://doi.org/10.1038/nature16961) (2016).
9. Jamison, K. W., Gu, Z., Wang, Q., Sabuncu, M. R. & Kuceyeski, A. Release the Krakencoder: A unified brain connectome translation and fusion tool, DOI: [10.1101/2024.04.12.589274](https://doi.org/10.1101/2024.04.12.589274) (2024).
10. Puig, J. *et al.* Magnetic Resonance Imaging Biomarkers of Brain Connectivity in Predicting Outcome after Mild Traumatic Brain Injury: A Systematic Review. *J. Neurotrauma* DOI: [10.1089/neu.2019.6623](https://doi.org/10.1089/neu.2019.6623) (2020).
11. Khatri, U. & Kwon, G.-R. Alzheimer’s Disease Diagnosis and Biomarker Analysis Using Resting-State Functional MRI Functional Brain Network With Multi-Measures Features and Hippocampal Subfield and Amygdala Volume of Structural MRI. *Front. Aging Neurosci.* **14**, DOI: [10.3389/fnagi.2022.818871](https://doi.org/10.3389/fnagi.2022.818871) (2022).
12. Bruin, W. B. *et al.* Development and validation of a multimodal neuroimaging biomarker for electroconvulsive therapy outcome in depression: A multicenter machine learning analysis. *Psychol. Medicine* **54**, 495–506, DOI: [10.1017/S0033291723002040](https://doi.org/10.1017/S0033291723002040) (2024).
13. Pathak, A., Roy, D. & Banerjee, A. Whole-Brain Network Models: From Physics to Bedside. *Front. Comput. Neurosci.* **16**, DOI: [10.3389/fncom.2022.866517](https://doi.org/10.3389/fncom.2022.866517) (2022).
14. Deco, G. & Kringelbach, M. L. Great Expectations: Using Whole-Brain Computational Connectomics for Understanding Neuropsychiatric Disorders. *Neuron* **84**, 892–905, DOI: [10.1016/j.neuron.2014.08.034](https://doi.org/10.1016/j.neuron.2014.08.034) (2014).
15. Herzog, R. *et al.* Neural mass modeling for the masses: Democratizing access to whole-brain biophysical modeling with FastDMF. *Netw. Neurosci.* 1–23, DOI: [10.1162/netn_a_00410](https://doi.org/10.1162/netn_a_00410) (2024).
16. Deco, G., Kringelbach, M. L., Jirsa, V. K. & Ritter, P. The dynamics of resting fluctuations in the brain: Metastability and its dynamical cortical core. *Sci. Reports* **7**, 3095, DOI: [10.1038/s41598-017-03073-5](https://doi.org/10.1038/s41598-017-03073-5) (2017).

17. Freyer, F. *et al.* Biophysical Mechanisms of Multistability in Resting-State Cortical Rhythms. *J. Neurosci.* **31**, 6353–6361, DOI: [10.1523/JNEUROSCI.6693-10.2011](https://doi.org/10.1523/JNEUROSCI.6693-10.2011) (2011).
18. Freyer, F., Roberts, J. A., Ritter, P. & Breakspear, M. A Canonical Model of Multistability and Scale-Invariance in Biological Systems. *PLoS Comput. Biol.* **8**, e1002634, DOI: [10.1371/journal.pcbi.1002634](https://doi.org/10.1371/journal.pcbi.1002634) (2012).
19. Hoffmann, J. *et al.* Training compute-optimal large language models. In *Proceedings of the 36th International Conference on Neural Information Processing Systems*, NIPS '22, 30016–30030 (Curran Associates Inc., Red Hook, NY, USA, 2024).
20. Barch, D. M. *et al.* Function in the human connectome: Task-fMRI and individual differences in behavior. *NeuroImage* **80**, 169–189, DOI: [10.1016/j.neuroimage.2013.05.033](https://doi.org/10.1016/j.neuroimage.2013.05.033) (2013).
21. Perl, Y. *et al.* Data augmentation based on dynamical systems for the classification of brain states. *Chaos, Solitons & Fractals* DOI: [10.1101/2020.01.08.898999](https://doi.org/10.1101/2020.01.08.898999) (2020).
22. Deco, G. *et al.* Resting-State Functional Connectivity Emerges from Structurally and Dynamically Shaped Slow Linear Fluctuations. *J. Neurosci.* **33**, 11239–11252, DOI: [10.1523/JNEUROSCI.1091-13.2013](https://doi.org/10.1523/JNEUROSCI.1091-13.2013) (2013).
23. Cabral, J., Kringelbach, M. L. & Deco, G. Exploring the network dynamics underlying brain activity during rest. *Prog. Neurobiol.* **114**, 102–131, DOI: [10.1016/j.pneurobio.2013.12.005](https://doi.org/10.1016/j.pneurobio.2013.12.005) (2014).
24. Watanabe, T. *et al.* Energy landscapes of resting-state brain networks. *Front. Neuroinformatics* **8**, 12, DOI: [10.3389/fninf.2014.00012](https://doi.org/10.3389/fninf.2014.00012) (2014).
25. Rabuffo, G., Fousek, J., Bernard, C. & Jirsa, V. Neuronal Cascades Shape Whole-Brain Functional Dynamics at Rest. *eNeuro* **8**, ENEURO.0283–21.2021, DOI: [10.1523/ENEURO.0283-21.2021](https://doi.org/10.1523/ENEURO.0283-21.2021) (2021).
26. Kancharala, V. K., Bhattacharya, D. & Sinha, N. Spatial Encoding of BOLD fMRI Time Series for Categorizing Static Images Across Visual Datasets: A Pilot Study on Human Vision. In *TENCON 2023 - 2023 IEEE Region 10 Conference (TENCON)*, 1117–1122, DOI: [10.1109/TENCON58879.2023.10322476](https://doi.org/10.1109/TENCON58879.2023.10322476) (2023).
27. Crossley, N. A. *et al.* Cognitive relevance of the community structure of the human brain functional coactivation network. *Proc. Natl. Acad. Sci.* **110**, 11583–11588, DOI: [10.1073/pnas.1220826110](https://doi.org/10.1073/pnas.1220826110) (2013).
28. Greicius, M. D., Krasnow, B., Reiss, A. L. & Menon, V. Functional connectivity in the resting brain: A network analysis of the default mode hypothesis. *Proc. Natl. Acad. Sci.* **100**, 253–258, DOI: [10.1073/pnas.0135058100](https://doi.org/10.1073/pnas.0135058100) (2003).
29. Niendam, T. A. *et al.* Meta-analytic evidence for a superordinate cognitive control network subserving diverse executive functions. *Cogn. Affect. & Behav. Neurosci.* **12**, 241–268, DOI: [10.3758/s13415-011-0083-5](https://doi.org/10.3758/s13415-011-0083-5) (2012).
30. Bernard, F. *et al.* The ventral attention network: The mirror of the language network in the right brain hemisphere. *J. Anat.* **237**, 632–642, DOI: [10.1111/joa.13223](https://doi.org/10.1111/joa.13223) (2020).
31. Biswal, B., Zerrin Yetkin, F., Haughton, V. M. & Hyde, J. S. Functional connectivity in the motor cortex of resting human brain using echo-planar mri. *Magn. Reson. Medicine* **34**, 537–541, DOI: [10.1002/mrm.1910340409](https://doi.org/10.1002/mrm.1910340409) (1995).
32. Themes, U. F. O. The limbic network: Influence over motor control, memory, and learning (2020).
33. Damoiseaux, J. S., Prater, K. E., Miller, B. L. & Greicius, M. D. Functional connectivity tracks clinical deterioration in Alzheimer's disease. *Neurobiol. Aging* **33**, 828.e19–30, DOI: [10.1016/j.neurobiolaging.2011.06.024](https://doi.org/10.1016/j.neurobiolaging.2011.06.024) (2012).
34. Klobušiaková, P., Mareček, R., Fousek, J., Výtvarová, E. & Rektorová, I. Connectivity Between Brain Networks Dynamically Reflects Cognitive Status of Parkinson's Disease: A Longitudinal Study. *J. Alzheimer's disease: JAD* **67**, 971–984, DOI: [10.3233/JAD-180834](https://doi.org/10.3233/JAD-180834) (2019).
35. Desikan, R. S. *et al.* An automated labeling system for subdividing the human cerebral cortex on MRI scans into gyral based regions of interest. *NeuroImage* **31**, 968–980, DOI: [10.1016/j.neuroimage.2006.01.021](https://doi.org/10.1016/j.neuroimage.2006.01.021) (2006).
36. Glasser, M. F. *et al.* The Minimal Preprocessing Pipelines for the Human Connectome Project. *NeuroImage* **80**, 105, DOI: [10.1016/j.neuroimage.2013.04.127](https://doi.org/10.1016/j.neuroimage.2013.04.127) (2013).
37. Smith, S. M. *et al.* Resting-state fMRI in the Human Connectome Project. *NeuroImage* **80**, 144, DOI: [10.1016/j.neuroimage.2013.05.039](https://doi.org/10.1016/j.neuroimage.2013.05.039) (2013).
38. Oostenveld, R., Fries, P., Maris, E. & Schoffelen, J.-M. FieldTrip: Open Source Software for Advanced Analysis of MEG, EEG, and Invasive Electrophysiological Data. *Comput. Intell. Neurosci.* **2011**, 156869, DOI: [10.1155/2011/156869](https://doi.org/10.1155/2011/156869) (2010).
39. Cabral, J. *et al.* Cognitive performance in healthy older adults relates to spontaneous switching between states of functional connectivity during rest. *Sci. Reports* **7**, 5135, DOI: [10.1038/s41598-017-05425-7](https://doi.org/10.1038/s41598-017-05425-7) (2017).

40. Button, K. S. *et al.* Power failure: Why small sample size undermines the reliability of neuroscience. *Nat. Rev. Neurosci.* **14**, 365–376, DOI: [10.1038/nrn3475](https://doi.org/10.1038/nrn3475) (2013).
41. Sejnowski, T. J., Churchland, P. S. & Movshon, J. A. Putting big data to good use in neuroscience. *Nat. Neurosci.* **17**, 1440–1441, DOI: [10.1038/nn.3839](https://doi.org/10.1038/nn.3839) (2014).
42. Han, X. *et al.* Reliability of MRI-derived measurements of human cerebral cortical thickness: The effects of field strength, scanner upgrade and manufacturer. *NeuroImage* **32**, 180–194, DOI: [10.1016/j.neuroimage.2006.02.051](https://doi.org/10.1016/j.neuroimage.2006.02.051) (2006).
43. Brown, G. G. *et al.* Multisite reliability of cognitive BOLD data. *NeuroImage* **54**, 2163–2175, DOI: [10.1016/j.neuroimage.2010.09.076](https://doi.org/10.1016/j.neuroimage.2010.09.076) (2011).
44. Roffet, F., Delrieux, C. & Patow, G. Assessing Multi-Site rs-fMRI-Based Connectomic Harmonization Using Information Theory. *Brain Sci.* **12**, 1219, DOI: [10.3390/brainsci12091219](https://doi.org/10.3390/brainsci12091219) (2022).
45. Bai, S., Kolter, J. Z. & Koltun, V. An Empirical Evaluation of Generic Convolutional and Recurrent Networks for Sequence Modeling, DOI: [10.48550/arXiv.1803.01271](https://doi.org/10.48550/arXiv.1803.01271) (2018). [1803.01271](https://arxiv.org/abs/1803.01271).
46. Kong, Q. *et al.* PANNs: Large-Scale Pretrained Audio Neural Networks for Audio Pattern Recognition, DOI: [10.48550/arXiv.1912.10211](https://doi.org/10.48550/arXiv.1912.10211) (2020). [1912.10211](https://arxiv.org/abs/1912.10211).
47. Sezer, O. & Ozbayoglu, M. Algorithmic Financial Trading with Deep Convolutional Neural Networks: Time Series to Image Conversion Approach. *Appl. Soft Comput.* **70**, DOI: [10.1016/j.asoc.2018.04.024](https://doi.org/10.1016/j.asoc.2018.04.024) (2018).
48. UZUN, S., Kaçar, S. & Arıciöğlü, B. Deep learning based classification of time series of chaotic systems over graphic images. *Multimed. Tools Appl.* **83**, 8413–8437, DOI: [10.1007/s11042-023-15944-3](https://doi.org/10.1007/s11042-023-15944-3) (2024).
49. Liu, Z. *et al.* A ConvNet for the 2020s. In *2022 IEEE/CVF Conference on Computer Vision and Pattern Recognition (CVPR)*, 11966–11976, DOI: [10.1109/CVPR52688.2022.01167](https://doi.org/10.1109/CVPR52688.2022.01167) (2022).
50. Howard, J. & Gugger, S. Fastai: A Layered API for Deep Learning. *Information* **11**, 108, DOI: [10.3390/info11020108](https://doi.org/10.3390/info11020108) (2020).
51. Yeo, B. T. T. *et al.* The organization of the human cerebral cortex estimated by intrinsic functional connectivity. *J. Neurophysiol.* **106**, 1125, DOI: [10.1152/jn.00338.2011](https://doi.org/10.1152/jn.00338.2011) (2011).

Data and code availability

Data used for this research can be downloaded from <http://doi.org/10.5281/zenodo.14508469>, and code to replicate the results is available on <https://github.com/FacuRoffet99/paper-hcp-tasks-hopf-bifurcation>.

Acknowledgements

F.R. receives financial support from a doctoral scholarship from the National Scientific and Technical Research Council (CONICET), Argentina. G.P. acknowledges support from grant PID2021-122136OB-C22 from the Ministerio de Ciencia e Innovación, Spain.

Author contributions

F.R., G.P. and G.D. developed the concept. F.R. designed and conducted the experiments. F.R. wrote the first draft of the manuscript. C.D. supervised the research. All authors reviewed and edited the manuscript.

Competing interests

The authors declare no competing interests.